Green Chemistry

PAPER

View Article Online
View Journal | View Issue

Cite this: *Green Chem.*, 2021, **23**, 3983

Understanding plasma–ethanol non-equilibrium electrochemistry during the synthesis of metal oxide quantum dots†

Dilli Babu Padmanaban, *[a] Ruairi McGlynn, [a] Emily Byrne, [b] Tamilselvan Velusamy, [a] Małgorzata Swadźba-Kwaśny, [b] Paul Maguire [a] and Davide Mariotti [a]

Plasma–liquid interactions are becoming increasingly interesting due to their key features such as non-faradaic, non-equilibrium behaviour as well as electron-driven reactions, therefore with potential strong impact for several promising applications. However, understanding reaction mechanisms initiated at the plasma–liquid interface is complicated by short timescales and spatial non-uniformities. Here we study a plasma–ethanol system that has general relevance to broaden our understanding of plasma interacting at the surface of a liquid. This plasma-electrochemical approach has been successfully used to synthesize a range of metal–oxide nanoparticles and quantum dots (QDs). While nanoparticles and QDs can be an end to this process, they can also be viewed as 'chemical probes' that help understanding the underlying and progenitor chemical reactions. We have therefore studied plasma–ethanol interactions during the synthesis of CuO QDs. The colloid was characterised by Fourier transform infrared spectroscopy, ultra-violet-visible spectroscopy, nuclear magnetic resonance spectroscopy and gas chromatography-mass spectrometry. Further, measurements for pH and other trace products were also carried out. The analysis shows the acidolysis of the ethanol electrolyte where hydrogen peroxide was found after the plasma process. A semi-quantification of Cu ions was carried out to confirm the anodic dissolution of the Cu metal foil. Thus, a detailed set of reactions are proposed and has been discussed in detail. Material characterisation relied on transmission electron microscopy and X-ray photoelectron spectroscopy which provided important and complementary information to corroborate chemical reaction paths.

Received 29th September 2020,
Accepted 4th May 2021

DOI: 10.1039/d0gc03291c

rsc.li/greenchem

Introduction

Early work in plasma–liquid chemistry hinted at great opportunities as Harada[1] demonstrated the formation of amino acids, the fundamental units of all life forms from a simple carbon source and ammonia gas. Similarly, experiments conducted by J. Gubkin[2] more than a century ago (reduction of aqueous silver to solid silver) are today highly relevant for materials synthesis. The excitement in coupling a highly non-equilibrium plasma environment with the liquid phase stems from the fascinating prospects of initiating chemical reactions and 'injecting' short-lived radicals through an interface,[3] which can open-up opportunities for new synthesis routes for established chemical products as well as synthesis of materials and chemicals that are not achievable by other routes.[4] Plasmas have demonstrated this capability in the gas-phase where kinetically driven reactions have led to important technological developments of the previous century (*e.g.* in the microelectronic industry). However, the requirement for low-pressure operation with plasmas has severely limited the possibility of interfacing these plasmas with most liquids.

Recent advancements in atmospheric pressure plasmas have made it possible to couple plasma with a much broader range of liquid environments therefore dramatically empowering non-equilibrium chemistry initiated through plasma–liquid interactions.[5,6] Plasma-induced non-equilibrium electrochemistry (PiNE) is therefore a fast-emerging discipline[3,7] at the interface between plasma science and wet chemistry, which is impacting a very broad range of applications, including plasma medicine,[8] water disinfection,[9,10] nanomaterial synthesis,[11,12] analytical chemistry,[13] and surface science.[14] The term "non-equilibrium" refers here to

[a]*Nanotechnology & Integrated Bio-Engineering Centre, Engineering Research Institute, Ulster University-Jordanstown, Belfast, UK.*
E-mail: db.padmanaban@ulster.ac.uk, pdillib@gmail.com
[b]*QUILL Research Centre, School of Chemistry and Chemical Engineering, Queen's University Belfast, UK*

†Electronic supplementary information (ESI) available. See DOI: 10.1039/d0gc03291c

electrochemical and chemical reactions taking place at the interface between a non-equilibrium gas-phase plasma and the liquid surface.

The plasma–liquid interface presents a dynamic environment with a wide range of physical and chemical properties acting on diverse timescales. It is for this reason, combined with the strong application drive and rapid technological implementation, that fundamental understanding of the mechanisms which underpin recent achievements and future prospects is still lagging. Nevertheless, many phenomena involved in PiNE could, in principle, be generalized to form a solid theoretical framework, as exemplified by early work by Denaro *et al.*,[15] who attempted to generalize some of the oxidizing mechanisms in 'glow discharge electrolysis'.

In the context of material synthesis, PiNE has now shown outstanding features in particular for nanomaterials[16] whereby generalized synthesis and surface engineering methods have been developed for metallic, metal–oxide and semiconductor nanoparticles.[17–19] Recent rapid progress in the field has shown the possibility of synthesizing a very broad range of materials, which are now being further integrated in more complex systems and application devices.[20,21] Our previous work has demonstrated the possibility of a generalized PiNE method to synthesize metal oxide NPs that relies on a solid metal sacrificial anode used within an ethanol solution. More specifically, we have been able to synthesize oxides from copper[22] cobalt,[23] nickel,[24] molybdenum[25] and zinc. Among the two most stable oxides of copper, monoclinic cupric oxide (CuO) is a familiar and versatile transition metal oxide that is used for a wide range of applications such as heterogenous catalyst,[26] electrode for solar cells[27,28] super capacitor[29] and others.[30–33] Also, CuO can be used successfully as a heterogenous catalyst or integrated into composites with other metal oxides for CO_2 reduction *via* photocatalysis.[34,35]

While we previously reported on the synthetic routes to form some of these NPs,[22,23,25] here we deepen our study to unravel the mechanisms involved in the synthesis. We focus on the evolution of CuO QDs and we identify reaction paths, which can be generalized to the describe a generic PiNE processes with metal anodes in ethanol. This study is therefore crucial for improving and optimizing NP synthesis as well as to contribute to a PiNE theoretical framework. In this contribution we study in detail reaction chemical paths originating at the plasma–ethanol interface during PiNE.

Synthesis of quantum confined metal oxide NPs, or quantum dots (QDs), has proven difficult for many methods. In the specific case of CuO, there are very few reports demonstrating synthesis of CuO QDs[36] as many synthesis approaches lead to larger particles (*i.e.* not quantum confined). Generally, CuO NPs can be synthesized with a variety of techniques.[37–40] However, most of these synthesis techniques rely on long and multi-step processes[41] and in some cases on the use of expensive and toxic chemical compounds such as surfactants, precursor salts, capping agents (see Table S1 in the ESI† for a full comparison). Essential to the synthesis are metal monomer precursors which are formed by repetitive units of molecular structures that can be linked together to form a metal oxide lattice during synthesis.[42] Our proposed method based on PiNE has several advantages. Firstly, a pure solid precursor is used for copper, while most other synthesis techniques would use copper salt and surfactants.[43–45] The use of pure precursors reduces the formation of by-product and therefore waste. Oxygen needed for the formation of CuO is supplied *via* ethanol and water in our PiNE process. We show how water and ethanol molecules 'catalytically' activate the formation of intermediate copper-based organometallic compounds. The synthesis therefore results in a 'green' cycle which uses solid metallic copper as precursor and forms CuO QDs with traces of iso-propanol as by-products. The possibility of producing CuO QDs essentially without any by-products or waste is unique compared to most other synthesis methodologies (see Table S1†) which require purification steps following the synthesis. These results unveil important details on the chemistry of PiNE systems that are fundamental to understand this emerging new NPs synthesis approach. Furthermore, our results do highlight opportunities for a much wider range of applications and disciplines which can find PiNE-activated chemical reactions useful to achieve reaction products otherwise not possible (*e.g.* pharmaceuticals, agrochemical, polymers, oleochemicals *etc.*).

Experimental section

Setup and description of plasma synthesis

A hybrid plasma–liquid electrochemical cell was operated with a direct current (DC) power source (max. 15 mA, 10 kV, Matsusada Precision Inc.). The cell configuration (Fig. 1) may

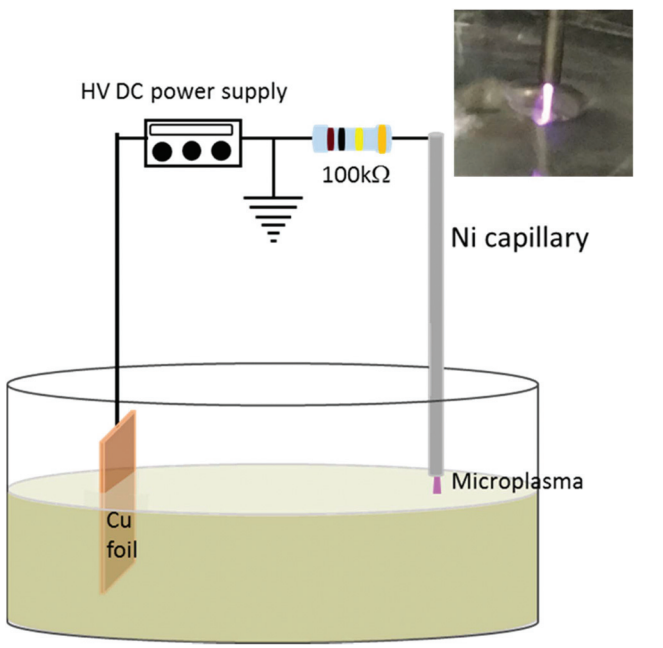

Fig. 1 Setup of the plasma–liquid electrochemical cell with Cu foil as anode, inset of a microplasma on liquid.

appear similar to a conventional electrochemical cell, however one of the solid electrodes, the cathode, is replaced with a plasma (the equivalent electrical circuit is also shown in Fig. S1 in the ESI†). Herewith a copper foil (Fisher scientific, thickness 100 μm, purity) was used as anode and immersed in ethanol electrolyte (conductivity <1 μS, purity 99.8%, Sigma Aldrich); the plasma cathode was generated from a hollow nickel capillary tube (0.7 mm internal diameter and 1 mm outer diameter). A 40 mL Pyrex glass beaker is initially filled with 5 mL of ethanol. The copper foil is immersed into ethanol by an area of 50 mm^2 and at a distance of about 15 mm from the nickel tube capillary. The tip of the Ni tube is placed 1 mm above the ethanol surface; the Ni capillary carries He gas at 50 standard cubic centimetres per minute (sccm; corresponding to a gas velocity of 2.16 m s^{-1}). A microplasma is ignited and sustained at the interface between the tip of the Ni capillary and ethanol. To compare and study the mechanisms involved, some of the experiments were also conducted with a graphite electrode replacing the copper foil (set up shown in Fig. S3†) but at the same processing conditions.

In the standard process a set voltage (3 kV) is applied for 30 min with a maximum current limit imposed. For the majority of our experiments, this limit was 0.5 mA while on occasion we have used a 3 mA current limit to support our analysis and discussion on the synthesis mechanisms. On application of the voltage, the ethanol conductivity increases due to the introduction of plasma-derived ionic species into the liquid and the current therefore increases, reaching the set limit after several minutes (~10 min at 0.5 mA set current) whereupon the applied voltage is then regulated (*i.e.* gradually reduced to 1.6 kV) to maintain a constant current (the current–voltage evolution at the different conditions is reported in Fig. S2 and S4 in the ESI†). As ethanol is a volatile solvent, its volume decreases due to evaporation and therefore to keep the capillary-liquid distance approximately constant the process (30 min in total) is halted for a few seconds every 10 min to allow for the addition of 1 mL of ethanol. The solution changes colour throughout the process and the final yellow solution obtained with copper foil as anode is related to the presence of CuO QDs, which is confirmed by further characterisation. The process has shown to be highly repeatable and reliable and resulting in the controlled synthesis of the QDs. The current batch-based set-up can produce 1.38 μg s^{-1}. However, we have already demonstrated in the lab the possibility of synthesizing CuO QDs in a modified continuous flow set-up with higher throughput.

CuO QDs characterization

Structure, crystallinity, and material phase of QDs were determined using a transmission electron microscope (TEM; JOEL, JEM-2100F) equipped with Gatan DualVision 600 Charge-Coupled Device (CCD) operated at an accelerating voltage of 200 kV. A 20 μL volume of CuO QD colloid was drop cast onto a gold coated carbon grid (400 mesh, #S187-4, Agar Scientific) with an ultra-thin carbon film (3 nm thick) and allowed to evaporate under ambient conditions and dried overnight. The lattice spacing of the crystal planes were estimated using ImageJ software.

X-ray photoelectron spectroscopy was carried out on samples obtained at different plasma processing time intervals and currents to identify changes in the materials composition. Measurements were performed using a Kratos Axis Ultra DLD photoelectron spectrometer working at ~10^{-9} mbar base pressure with monochromatic X-ray radiation Al Kα generated at 15 kV and 10 mA. The Cu 2p spectra were acquired with analyser pass energy of 20 eV, 0.05 eV steps, 142 ms dwell time. Samples were prepared by immersing the conductive graphite substrates (~98% purity) into the synthesized solutions and drying them slowly at room temperature (~21 °C) overnight. The position of the peaks were in general identified using NIST web database[46] and local database from CASA XPS software wherein the spectral fitting was also performed.

Optical transmittance of CuO QD colloids were studied by ultraviolet–visible (UV–Vis) spectroscopy with a PerkinElmer-Lambda 650S UV–Vis spectrometer fitted with a 150 mm integrating sphere. The absorbance of as prepared CuO colloids was measured in a quartz cuvette with a 1 cm path length.

Plasma processed liquid characterization

The Cu ion concentration in plasma processed ethanol was semi-quantitatively estimated using "Quantofix™" test strips. The sampling area of the test strip were immersed into the processed ethanol, removed and dried for 1–2 min. The resulting change of colour provides a quantitative indication of the Cu^{+}/Cu^{2+} ion concentration in the solution using the standard concentration colour chart provided with the strips.

Fourier transform infrared (FTIR) spectroscopy measurements of the processed colloids were carried out using Thermofisher Nicolet iS5 in order to identify species present in the liquid phase. The spectra were recorded from a liquid cell made up of BaF_2 window spaced by a PTFE film (thickness 50 μm) combined to form a small compartment. Approximately 20 μL of plasma-processed liquid were injected into the compartment ensuring that no air bubbles were formed. The liquid cell was then analysed in the transmittance mode and all the measurements were carried in nitrogen atmosphere to suppress interference of atmospheric water and carbon-di-oxide vibrational peaks in the spectra. All FTIR measurements were carried out within 5 minutes after the plasma process.

The pH of plasma processed liquids was tested using a handheld pH probe meter (Extech EC500, 0.01% pH resolution, range up to 14 pH). Before each measurement, the pH meter is calibrated with standard pH solution of 4 pH, 7 pH and 11 pH. The measurements are performed by placing the pH bulb into the plasma processed liquid.

The plasma-processed samples were studied with proton (^1H) and carbon (^{13}C) nuclear magnetic resonance (NMR) spectroscopy, as neat liquids with deuteriated dimethyl sulfoxide (DMSO-d_6) as an external lock. Bruker Avance DPX 600 MHz spectrometer was used in all measurements; 64 scans were recorded for ^1H NMR spectra and 2048 scans for ^{13}C NMR spectra.

Gas chromatography-mass spectrometry (GC-MS) studies were carried out on neat plasma-processed samples using Agilent Technologies 7890B GC system equipped with an Agilent Technologies 5977A MSD with Agilent Technologies HP-5MS UI 0.25 micron 30 m × 0.250 mm column attached. A quality chromatogram was produced by the samples diluted with toluene at a dilution factor of 10 to allow for well-resolved peaks for chemical compounds.

Colorimetric determination of hydrogen peroxide (H_2O_2) was carried on plasma processed ethanol. This is performed by mixing titanium oxy-sulphate scavenger (27–31% H_2SO_4 containing ~5% Ti basis, Sigma Aldrich) with plasma processed ethanol in the ratio of 1 : 2. Optical absorbance on the resultant solution was measured using UV–Vis spectroscopy in the range from 375 nm to 550 nm. Prior to the actual sample measurement, a standard calibration curve was produced with different known amount of hydrogen peroxide in ethanol. The concentration of H_2O_2 in the different plasma processed solution is calculated from the calibration curve and observed intensity of absorbance at 407 nm from the samples.

Plasma optical emission spectroscopy (OES) was carried out using an Ocean Optics USB 4000 spectrometer (200–1100 nm range) with 3648-element CCD array detector. For enhanced light collection from the microplasma, a collimator capped fibre optic tip is placed at distance ~7 mm from the plasma and angle 45° to the plane of liquid surface. All the spectra were recorded with integration time of 100 ms, averaged over 10 scans and corrected for electrical dark.

Results and discussion

Characterization after CuO QDs synthesis

Fig. 2a and b show transmission electron micrographs revealing well-dispersed and crystalline CuO QDs (synthesized at 0.5 mA). These are optimized synthesis conditions that lead to pure CuO QDs with negligible amounts of by-products. For instance, synthesis at 3 mA shows the presence of the Cu_2O phase and of amorphous clumps believed to be synthesis by-products (see ESI, *e.g.* Fig. S7a and b†). The size distribution for >130 particles is found to be relatively narrow (lower inset of Fig. 2a) and the lognormal curve fitting gives a particle mean diameter of 3.27 nm for 0.5 mA processing current. The selected area electron diffraction (SAED) patterns (upper inset of Fig. 2a) show circular bright and dark fringes indicating the diffraction from CuO crystal planes; samples prepared at 0.5 mA show dots arranged in circles ascribed to crystal planes (1 1 1), (−1 1 2), (0 2 2) and (0 2 3). The high-resolution image (Fig. 2b) show diffraction fringes which also support *d*-spacing values of 0.195 nm, 0.225 nm, 0.247 nm, 0.230 nm, 0.270 nm related to crystal planes of (−1 1 2), (1 1 1), (0 0 2), (2 0 0) and (1 1 0) of CuO crystal structure respectively.

XPS analysis confirms the CuO QDs chemical composition (Fig. 2c). The survey scan confirms the presence of Cu and O from the CuO QDs and some surface carbon environmental contamination. The core Cu 2p were deconvoluted mainly into

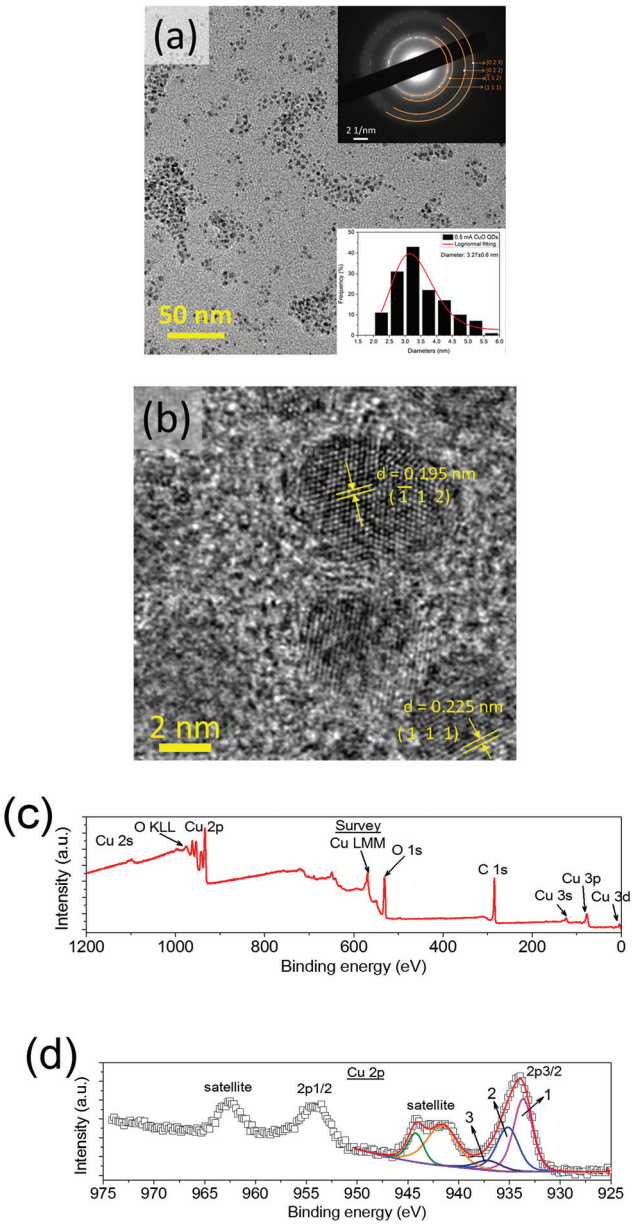

Fig. 2 Structure and chemical composition of CuO QDs synthesized at 0.5 mA: (a) transmission electron micrographs with SAED and particle size distribution (insets), (b) high resolution image (c) XPS survey scan spectra and (d) XPS high resolution Cu 2p core level.

peaks 1, 2 and 3 (Fig. 2c) corresponding to CuO (933.6 eV), Cu complexes such as $Cu(OH)_2$ or $Cu(OCH_2CH_3)_2$ (935.1 eV) and Cu^{2+} octahedrally coordinated by oxygen species (937 eV),[47,48] respectively. Above 940 eV, the two Cu^{2+} satellites (942.5 eV and 962.5 eV) are also present. The strong CuO peak with the corresponding satellites is strong evidence of the CuO phase where various Cu complexes can be associated with surface terminations as well as minor residual intermediate products (see discussion further below). We should note that Cu_2O does not produce satellite peaks but a peak at 931.4 eV,[49] which we were unable to fit and this therefore confirms the purity of the CuO QDs.

In addition to the QDs, we have also characterized the solution after 30 min processing. We have first verified the supply of Cu precursor from the copper foil anode. The Cu ion concentration after the 30 min process was evaluated with Cu ion test strip, which indicate a value above 30 mg L^{-1}. These measurements confirm anodic ion dissolution from the Cu foil and a more in-depth and time-dependent analysis is provided below. The concentrations of hydrogen peroxide and water were also measured, and these were estimated to be in the range of 0.5–1.0 mM and 12 mM respectively, after 30 min processing.

Fig. 3 shows the FTIR transmittance observed from 4000 cm^{-1} to 750 cm^{-1} for the ethanol solution after CuO QDs synthesis at 0.5 mA (see ESI Fig. S8,† 3 mA) and compared with untreated ethanol. These measurements were initially carried out by placing the samples on the diamond window in the attenuated total reflectance (ATR) module which records the spectrum from 550 cm^{-1} to 4000 cm^{-1}. Spectra were recorded averaging 30 scans after background removal. The broad absorption peak at 3100–3600 cm^{-1} corresponds to O–H stretching vibrations modes. The peaks at 2973 cm^{-1} and 2888 cm^{-1} are due to the C–H stretching vibrations. Peaks at 1089 cm^{-1} and 1335 cm^{-1} are from C–C stretching and CH_3 bending respectively and these bands were commonly observed in all the samples with no visible differences.[50] This is consistent with ethanol constituting the majority of the liquid samples after the plasma treatment, *i.e.* no detectable by-products with this analytical method.

A more detailed analysis of the solution can be conducted with NMR and GC-MS. Fig. 4a shows the ^1H NMR spectra of plasma-processed samples at 0.5 mA. In order to understand better the mechanisms taking place at the plasma–ethanol interface, we have carried out additional experiments where we have replaced the Cu foil electrode with a graphite electrode; this arrangement, while preserving the same conditions at the plasma–liquid interface, prevents the supply of Cu precursor and the formation of CuO QDs. Pure and untreated ethanol is also shown for comparison. All samples (*i.e.* ethanol reference and samples after processing with Cu electrode and with graphite electrode) show three significant peaks around 1.18 ppm (triplet), 3.61 ppm (quartet) and 5.20–5.35 ppm (singlet) which are identified to three different proton environments that match to CH_3, CH_2 and OH in ethanol molecule, respectively.[51] The small symmetrical satellite peaks either side of the 1.18 ppm and 3.61 ppm peaks are due to ^{13}C nuclei coupling. Ethanol processed from graphite anode displays a peak at ~3.93 ppm, that could be attributed to secondary carbon (CH) group of isopropanol (IPA) molecule. We should note that this peak had higher relative integration area for the higher current (3 mA, Fig. S9 in ESI†) and when the graphite electrode is used. The signal above 5 ppm has changed from that of neat ethanol in both plasma-treated cases: it became broader after plasma processing with the graphite anode (this suggests dynamic exchange between several environments) and shifted after plasma processing with the Cu anode. As two other compounds with labile protons generated are present after plasma processing, *i.e.* isopropanol and water, this means that water, ethanol and isopropanol will exchange their OH protons in a dynamic fashion contributing to broadening and/or shifting in the ^1H NMR signal from the OH group. Finally, a minor peak around 2.5 ppm comes from dimethyl sulphoxide (DMSO), which was used as the external lock.[52,53]

Fig. 4b shows the ^{13}C NMR spectra of plasma processed liquid samples with Cu and graphite anodes. The very small peaks are due to noise level intrinsically present in the spectra. The spectra mainly have two large peaks due to ethanol at 16.8 ppm and 56.3 ppm, which can be linked to terminal CH_3 and $-CH_2-$ groups respectively. The multiple corresponding to the deuterated DMSO is at 40 ppm. The sample with the graphite anode shows two peaks at 23.8 ppm and 62.7 ppm associated to methyl (CH_3) and secondary (–CH–) carbon in isopropyl alcohol (IPA), respectively.[50,52,53] Thus, ^{13}C NMR confirms that for the most part the solution consists of ethanol with some minor impurities, potentially IPA that is mainly formed with the graphite electrode, *i.e.* without the supply of Cu ions.

Fig. 5 shows the gas-chromatography-mass spectroscopy (GC-MS) chromatograms of samples processed with the Cu and graphite anodes for 0.5 mA (see Fig. S10 in ESI† for 3 mA). All the plasma processed samples show peaks of elution time related to ethanol at around 1.64 min with some minor peaks at 1.47 min, 1.52 min, 1.85 related to N_2, H_2O and dichloromethane respectively.

However, the sample with the graphite electrode also shows a peak following ethanol at higher elution time around 1.73 min corresponding to isopropyl alcohol. The ratios of integration area under the peaks are related to the ratio of the compounds present in the samples; while IPA was not present when the Cu foil was used, the process with the graphite

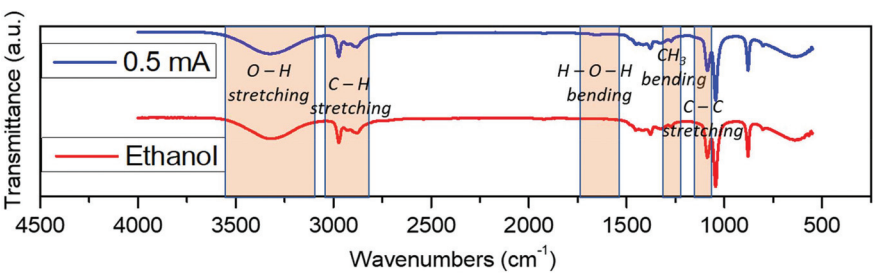

Fig. 3 Infrared transmittance of plasma processed ethanol at 0.5 mA, Cu anode in comparison with untreated ethanol.

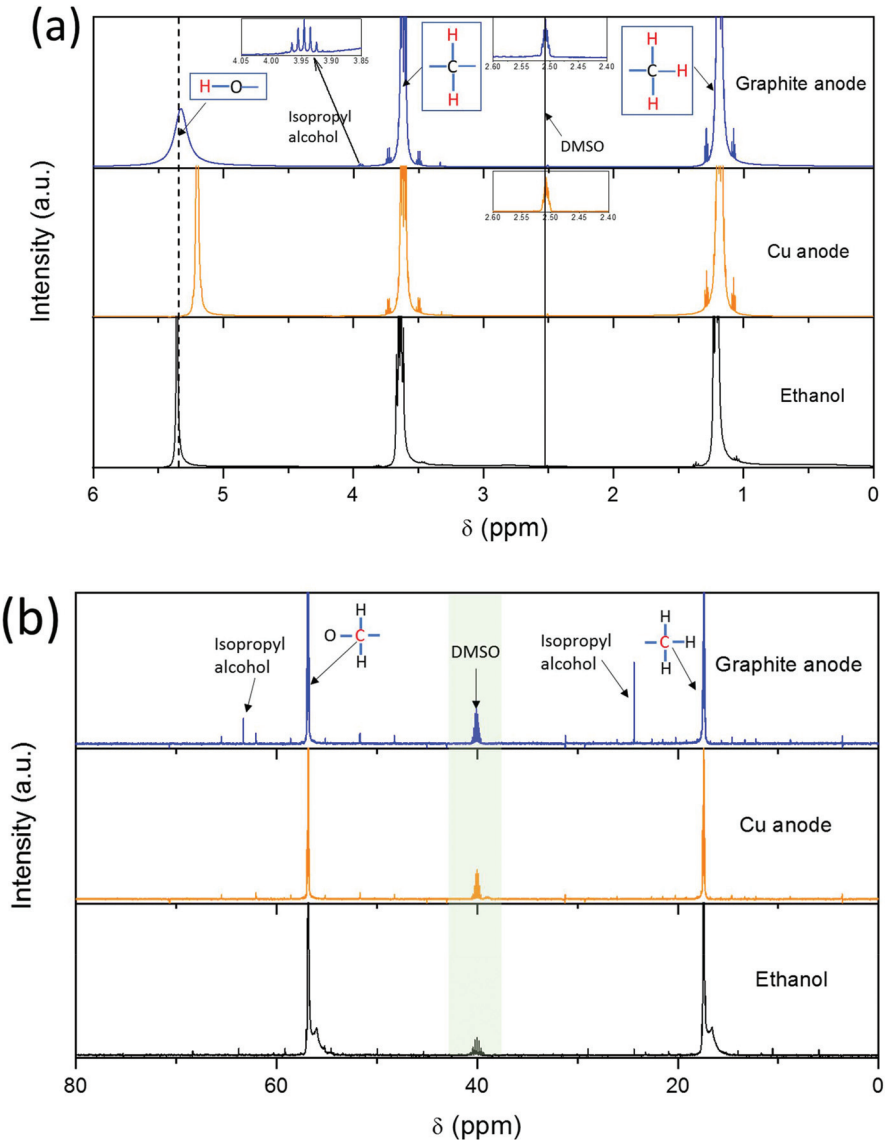

Fig. 4 NMR studies of plasma processed ethanol at 0.5 mA current treated for 30 minutes: (a) ^{1}H NMR and (b) ^{13}C NMR spectra. Each figure reports the spectra for pure ethanol, plasma treatment with copper foil and graphite anodes.

anode produced 38 : 1 ethanol : IPA concentration (see also Table S2 in ESI†). We should note that at higher current (3 mA), the results are fully consistent with the results produced at 0.5 mA; however, the higher current does produce a higher concentration (8 : 1) of the IPA also noticeable when the Cu foil is used (7 : 1), see ESI.†

The results presented so far indicate that pure CuO QDs are the main final products of the 30 min process. The solution, after synthesis, mainly consists of ethanol with possible traces of IPA by-product. Cu ions, water and hydrogen peroxide are also formed and used as it will be discussed further below.

Time evolution of the synthesis process

In order to understand better the synthesis mechanisms, the time evolution of the process was analysed with measurements carried out at various stages of the process within the 30 min. XPS analysis was carried out on the CuO QDs synthesized at different times (see ESI and Fig. S11† for full XPS details) and deconvoluted as previously described (Fig. 2d). The time evolution of relevant chemical species is shown in Fig. 6a. The peak intensity associated with CuO increases quickly at the expenses of other Cu complexes that are decreasing, *i.e.* Cu $(OH)_2$ or $Cu(OCH_2CH_3)_2$. This suggests an initial transient stage (<10 min) where the concentration of CuO QDs is still very small and where the supply of other chemical species is higher. In a second stage, where the various supply/consumption channels reach equilibrium, CuO QDs are fully developed and produced continuously; the trends resemble the electrical characteristics of the process. When the process is carried out at 3 mA (ESI, Fig. S12†), the supply of chemical species is

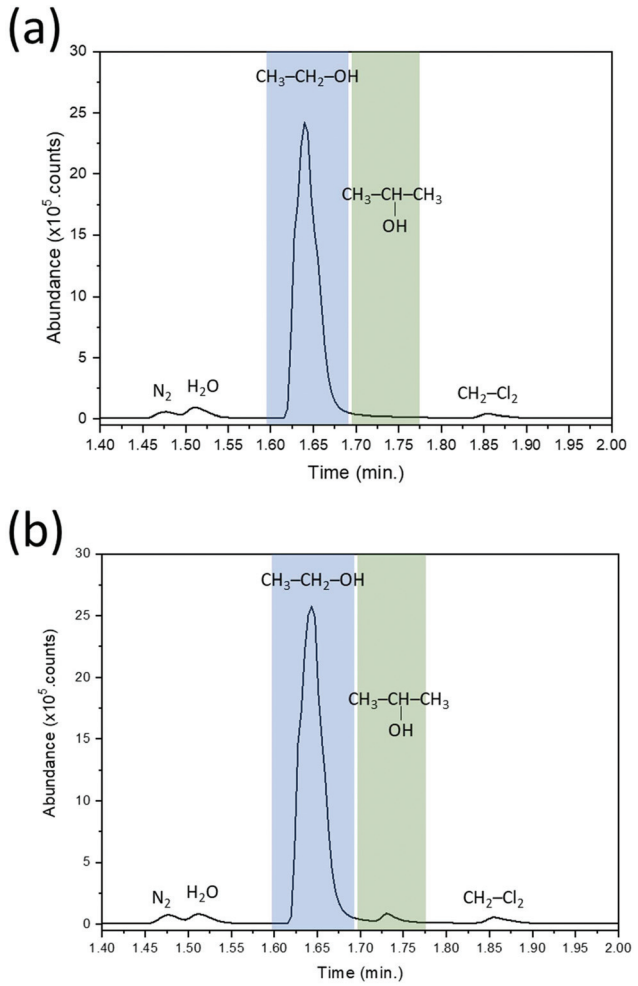

Fig. 5 Chromatogram of plasma processed ethanol at 0.5 mA, (a) Cu foil, and (b) graphite as anodes.

faster than the formation of CuO QDs and by-products are present in higher concentrations without reaching an equilibrium stage; in this case Cu_2O phase is also produced.

Fig. 6b show the evolution of Cu ions over different process interval at 0.5 mA for longer durations. The process of anodic dissolution is based on an electrochemical oxidation reaction that takes place on the surface of the Cu anode, which results in Cu ions released in solution and electrons flowing in the circuit aided by an external power supply.[54] This is represented by eqn (1) and (2) below.

$$Cu_{metal} \rightarrow Cu^{+} + e^{-} \quad (1)$$

$$Cu^{+} \rightarrow Cu^{2+} + e^{-} \quad (2)$$

However, dissolution of Cu ions is generally accompanied with formation of Cu complex with solvent molecules which is reported by Abbott *et al.* with metal ion.[55] We also observed that the Cu ion concentration increases over longer plasma process time as measured for two different plasma current as shown in the ESI (Fig. S13c†). Further, the formation of Cu complex and their evolution to CuO in ethanol will be discussed in detail in the reaction mechanism section.

Fig. 6c shows the absorbance and estimated bandgap values for different process intervals; the bandgap values were estimated assuming an indirect bandgap. Similar absorbance and Tauc's plots of the colloids at 3 mA are included in the ESI (Fig. S14†) for completeness. As the process time increases, the absorbance curve also increases (Fig. 6c); however, in the Tauc plot, the intercept for different interval remains constant at ~2 eV (inset of Fig. 6c, see ESI Fig. S14 and S16†), which suggests that longer synthesis time contributes to the increased number of QDs without affecting other features such as size or composition.

Hydrogen peroxide (H_2O_2) is known to be generated in a range of PiNE processes. The exact location and timing of dissociation, species diffusion from plasma to liquid and formation of hydrogen peroxide is however still under debate and in some cases could depend from the specific process/plasma set-up being used (see also section 9 in ESI†). Fig. 6d shows the H_2O_2 concentrations in ethanol after the synthesis of the CuO QDs (see ESI† for details on the experimental procedure to measure H_2O_2). These results confirm that H_2O_2 is produced in our process and its concentration increases slowly throughout. Subsequently, in order to determine if H_2O_2 participates in the reactions leading to CuO QDs synthesis, we have replaced the Cu foil electrode with a graphite electrode; this arrangement while preserving the same conditions at the plasma–liquid, prevents the supply of Cu precursor and the formation of CuO QDs. The concentration of H_2O_2 with the graphite electrode (Fig. 6d) increases linearly with time, while with the Cu foil, an initial linear increase reaches saturation after ~20 min. This suggests that when the CuO QDs are produced, H_2O_2 is consumed and therefore participate at some level in the reactions leading to the synthesis of the QDs. At high current (3 mA, see ESI Fig. S20†), the H_2O_2 concentration increases even further with the graphite electrode while its consumption in the reactions involving Cu-complexes is even more obvious.

The pH is also a key parameter that can dramatically change the reaction paths. Fig. 6e shows the variation of pH after ethanol exposure to the plasma where also in this case we have evaluated the process with Cu foil and graphite electrodes. In both cases the pH decreases at a fast rate in the first 5 min and then more slowly for the remaining of the 30 min process. The plasma interacting with ethanol in ambient air and with a Cu foil anode induces changes in the pH from 7.3 pH to about 5.2 pH. In comparison, when the process was carried out with a graphite rod anode, the pH was reduced to 4.8 pH. A higher current (3 mA), the process shows similar trends, although a more dramatic pH reduction is observed when the graphite electrode is used (<3 pH) (see ESI, Fig. S21†); pH and H_2O_2 measurements suggest that the process at 3 mA with the graphite electrode reaches stages where the reaction chemistry evolves even further. Several studies have been carried out on acidolysis of the electrolyte during a plasma process, however these are often related to

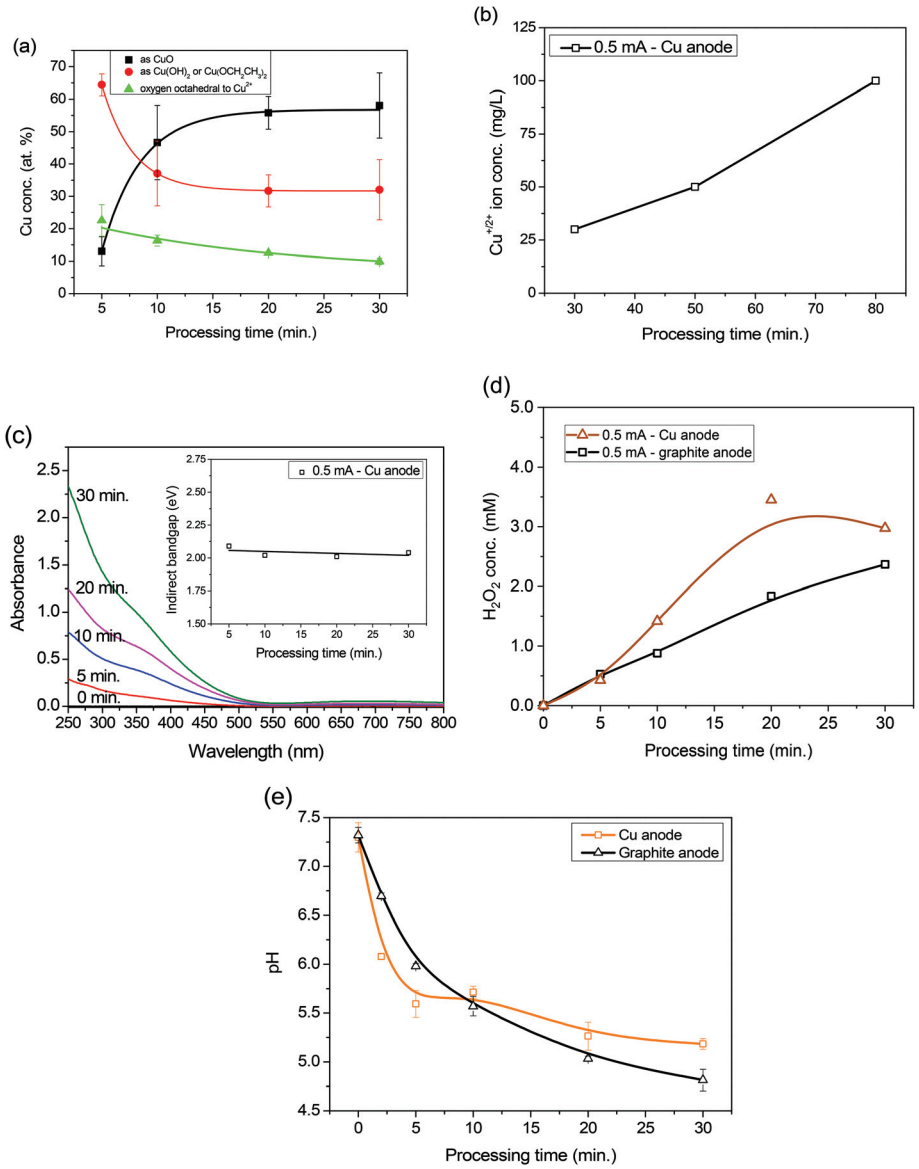

Fig. 6 Time dependant analysis from plasma processed liquids with Cu foil anode in comparison with graphite anode at 0.5 mA. (a) Quantification of Cu^{2+} mainly as oxide and its monomer form at 0.5 mA current where error bars are estimated from 3 sample spots. (b) Estimated $Cu^{2+/+}$ ion concentration. (c) Absorption spectra with Cu anode with inset show the calculated bandgap. (d) Hydrogen peroxide and (e) variation of pH with (errors bars related to three different measurements) for various plasma process intervals determined in the solution.

water in air plasmas.[9,56–58] Oehmigen *et al.* reported that aqueous medium pH changes can be from nitric acid/nitrous acids formed through the plasma process.[9] Other reports have linked increased acidity to the presence of O_2^- superoxide anion formed from the plasma process ($e^- + O_2 \rightarrow O_2^-$).[59] Further reports have attributed the acidity of water to H_3O^+ species resulted from electron and He ion impact reaction with water molecule.[60,61] The presence of H^+ radical which can also influence the pH in ethanol is attributed also to ion induced dissociation of water molecule.[9]

To resolve any smaller changes in the ethanol solution after the plasma process, FTIR measurements were carried out using a liquid cell placed in the transmittance module (ESI, section 11†). In these results, we observed a well-defined weak band at around 1658 cm^{-1} which changes with plasma processing time (ESI, Fig. S23 and S24†). The peak at 1658 cm^{-1} corresponds to H–O–H bending modes of a free H_2O molecule,[62] which suggests an increasing water content during plasma processing. Based on a calibration curve of known amount of water in ethanol (shown in Fig. S22 in ESI†), the concentration of water content after the plasma process for two different anodes and durations were estimated as shown in Fig. 7. The comparison between the results produced with the graphite anode and the Cu anode indicate that when the Cu foil is used, a slightly lower concentration of water is obtained. Water is likely to originate from water vapour dis-

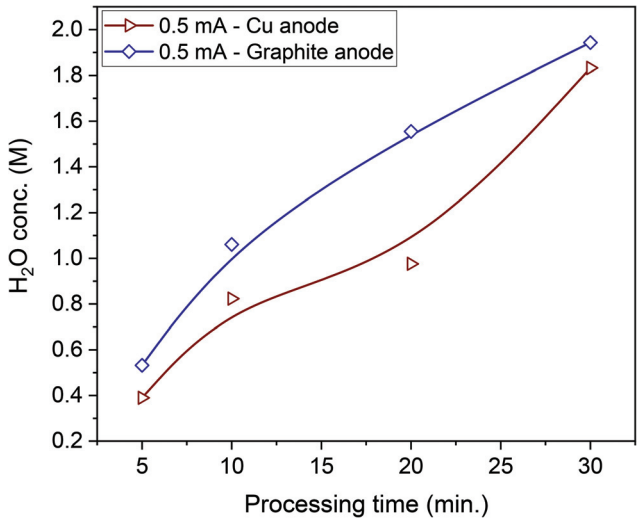

Fig. 7 Quantified water molecule content in plasma processed ethanol at 0.5 mA.

solution in ethanol when exposed to air.[63] Again our results at higher current (see ESI, Fig. S25†) further confirm previous results that processing at 3 mA lead to a chemical environments that drastically differ and as previously noted do not lead to the same purity for CuO QDs.

Description and analysis of the reaction mechanism

Plasma interactions with ethanol in air induce different types of chemical reactions through the interface producing several species. Studies on plasma interactions with water have found that ions and radicals such as H_3O^+, O_2^-, OH*, NO_2^-, NO_3^- *etc.* have been created or supplied to the liquid phase.[64] In our configuration, electrons are also expected to arrive at the liquid surface and become solvated, thereafter playing a significant role in a range of reactions. Counter ions present in the liquid are expected to move towards the region of their respective electrode. Almubarak *et al.*[65] reported that with glow discharges in aqueous ethanol, products such as acetaldehyde, hydrogen peroxide, butan-2,3-diol, and acetic acid were formed at varying concentrations depending on a range of parameters such as oxygen gas flow, discharge current and voltage used. Du *et al.* reported that with tornado-type electrical discharge,[66] arc discharge plasma reactor,[67] plasma-catalyst hybrid systems,[68] hydrogen gas and carbon monoxide are the major products in addition to other minor components such as aldehyde, acetic acid, methane, *etc*. However, the plasma configuration and conditions can drastically impact the reaction chemistry and importantly the kinetics of reaction paths so that different products can easily result from different plasma set-ups.

Based on our results we can draw conclusions on the species present in the samples after the plasma treatment at different conditions and on the likely species that may be formed during the process. Overall, we could not find acetaldehyde or acetic acid in significant quantities as was observed in the glow discharge electrolysis process.[65] Instead NMR and FTIR spectroscopies, as well as GC-MS measurements, reveal the main species to be ethanol and of course CuO QDs as demonstrated through our TEM and XPS materials characterization. The process does produce hydrogen peroxide and water (Fig. 6d and 7); however, their production and consumption reach a steady-state with a relatively low concentration throughout the process. Acidolysis of ethanol was also observed over the process time. As per our results and analysis below, no other species formed at or introduced through the interface contribute to the formation of CuO QDs.

These results can now be used to draw a picture of the possible formation mechanisms leading to CuO QDs (Fig. 8), which mainly relates to the reactions cycle once steady state is reached, *i.e.* after the initial transient stage (>10 min). For the most part, the initial solution remains unchanged where ethanol essentially acts as a "catalyst" and the process can be described as a "green" reaction cycle with water molecule and other by-products such as H_2O_2 acting in support of the synthesis. We should note that spatial variation in the liquid volume exists and in general we expect the concentration of plasma-induced radicals/ions to peak at the plasma–ethanol interface and to decrease with distance into the bulk liquid. As a first-order approximation we can consider a small liquid volume ('reaction volume') underneath the plasma–ethanol interface, where CuO QDs nucleation and growth is believed to take place. CuO QDs, after synthesis, are then expected to move out the reaction volume and into the bulk of the liquid, which in turn also supplies and exchanges various chemical species. A diagram depicting the overall process is provided in Fig. 8 (step-1 to step-4).

Step-1a – At the plasma–ethanol interface, gas phase electrons interact with and dissociate ethanol molecule either at the interface or as solvated electrons. This dissociation forms ethoxy ions ($CH_3CH_2O^-$) and hydrogen radicals (step-1a of Fig. 8) and occurs either *via* dissociative electron attachment of vaporized ethanol molecules or through the reaction of solvated electrons with ethanol in the liquid phase. The hydrogen radicals then recombine and form molecular hydrogen gas, which is released to the atmosphere. While we do not have direct proof for these reactions, the literature provides ample evidence that these pathways are realistic and occurring;[69,70] more important is that these electron-induced reactions are corroborated with our experimental measurements on the resulting cascaded chemistry as discussed here below.

Step-1b – Near the anode area at the copper foil (step-1b), anodic dissolution occurs and results in the production of Cu ions (standard oxidation potential for Cu^{2+} ion is −0.345 V)[71] into the solution. This is evidenced by the presence of Cu ions supported from semi-quantitative analysis using the copper test strips (Fig. 6b). The concentration of copper ions was found to increase with processing time up to ~30 mg L^{-1} and also with processing current (ESI, Fig. S13c and Table S3†). The increasing concentration in all cases is consistent with anodic dissolution and indicates that more Cu is supplied than it is consumed and therefore QDs synthesis is not limited

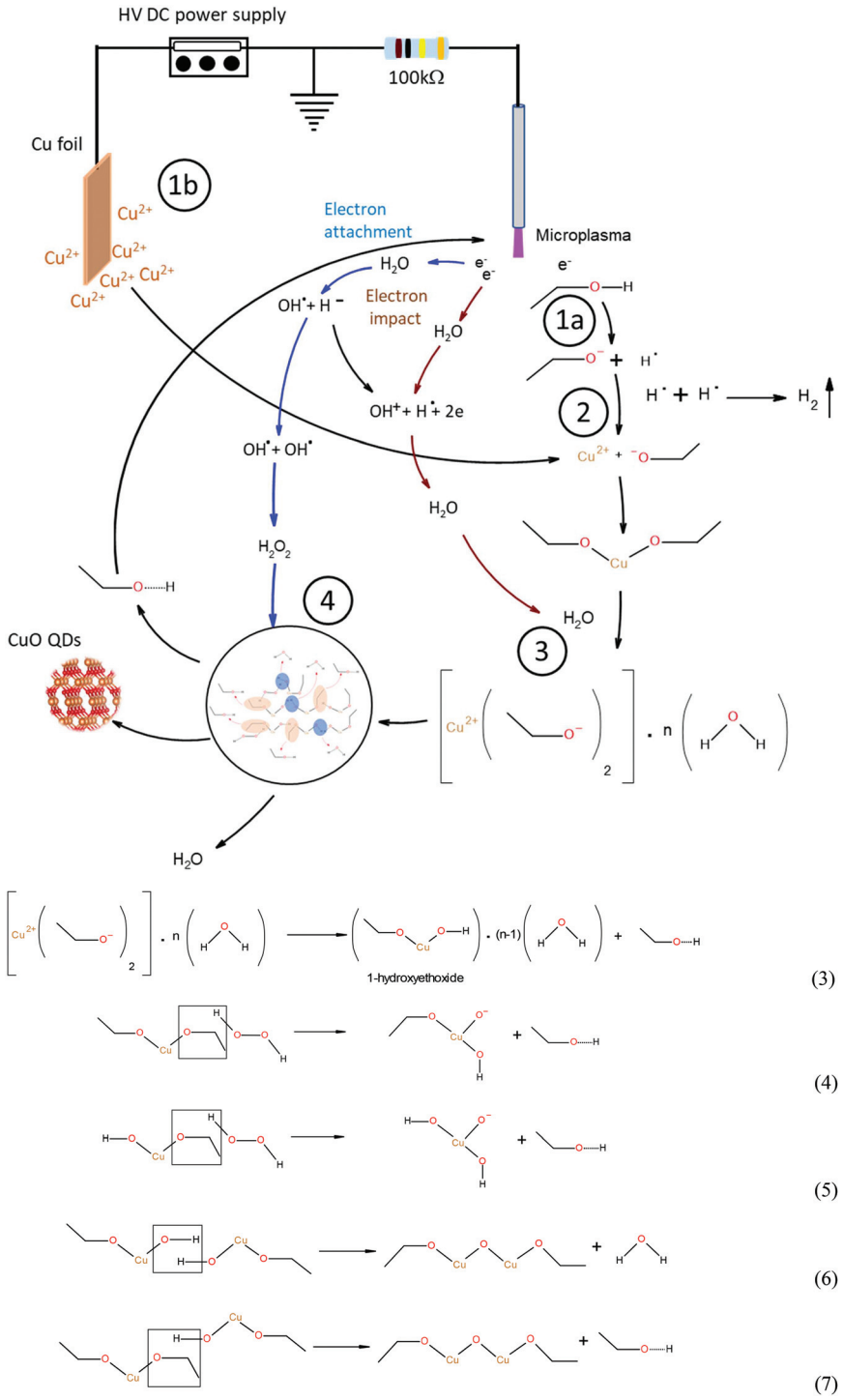

Fig. 8 Reaction cycle and equation involving the formation of CuO QDs, where blue and brown coloured arrows represent the mechanism occurs at the interface and black cycle corresponds to reaction inside ethanol.

by the supply of Cu. The divalent Cu ions (Cu-II) are then transported *via* electrophoresis towards the plasma–ethanol interface, whereas the monovalent state (Cu-I) is not believed to contribute significantly to the current as it is less soluble in ethanol. Surface passivation in the form of an insulating film on the electrode could affect anodic dissolution, however this is not observed and at low currents this is not expected to affect the dissolution.[55]

Step-2 – The negatively charged ethoxy ions then react with the electropositive Cu-II ions to form copper ethoxide as in step-2 (Fig. 8). This is in part supported by our XPS analysis and peaks related to Cu-complexes that would be present in

copper ethoxide. The XPS results show that these groups are formed very rapidly at the start of the process (Fig. 6a) and then decrease until steady state is reached and CuO QDs are being formed continuously; this is fully consistent with copper ethoxide and its role played in the synthesis of the CuO QDs. Of course, our most direct evidence that corroborates the copper ethoxide being an intermediate product is the formation of CuO QDs. We should note that if copper ethoxide is formed and participates in the QDs synthesis, it may be fully consumed and therefore we would not expect this compound to be detected. If copper ethoxide residues were instead observed, it would indicate a supply in excess of what was needed for CuO QD synthesis. The results produced at 3 mA are also supporting this interpretation as also in this case the XPS of Cu complexes and CuO follow opposite trends, *i.e.* CuO peak growing and Cu complexes decreasing (Fig. S12 in ESI†).

Step-3 – Water molecules (as revealed from FTIR measurements) present in ethanol can react with copper ethoxide to form a gel. Such a process of gelation was commonly observed when metal alkoxides reacts with water as reported by Lee *et al.*[72] Similarly in our process, a gelation occurs through hydrolysis (step-3 in Fig. 8). Sol–gel is a well-known technique for the synthesis of inorganic and ceramic glasses.[73] In another example, Yoldas[74] observed gelation of titanium alkoxides to intermediate oxide at different conditions with water and hydrogen peroxide. The author noted that H_2O_2 reacts rapidly with hydrolysed products by altering the terminal alky to hydroxy or oxy-bridges. Thus, hydrolysis affects the structure of gel molecules and modifying structure and shape of nanoparticles. These condensates are composed of molecular complexes with coordinated bonds and ligands. Cudennec *et al.*[75] reported that $Cu(OH)_2$ in aqueous medium at 323 K is present as tetrahydroxocuprate (II) anions, $Cu(OH)_4^{2-}$, a complex of divalent Cu ion with OH at the corners of a square planar structure. Likewise in our PiNE process, water, Cu ions and ethoxy ions are expected to form a distorted octahedral complex with the Cu-II ion at the centre, similar to the one reported by Brubaker *et al.*[76] It was also explained that this was a reversible transformation which depends on the copper ion concentration and it stabilises on account of Jahn Teller distortion that later transforms it to monoclinic CuO. The Cu-II ion at d^9 state is under Jahn Teller distortion and can stabilise itself in square planar geometry depending on the type of ligands and bonding between them. An intermediate stage of the copper ethoxide undergoes partial hydrolysis with water molecules to form a complex as shown in eqn (3) (step 4 in Fig. 8). Abbott *et al.*[55] in their study of anodic dissolution of metals, stated that the speciation of metal complexes relies on concentration and the coordinating nature of ligand and pH. The hydrolysis between the copper ethoxide and water molecules results in a Cu complex that later forms a localised cluster of gels. However, hydrogen peroxide enhances the growth of nanoparticle through per-oxy termination (O_2^{2-}) to metal atom as shown in eqn (4) and (5). Peroxyl groups are strong chelating agents that enhances hydrolysis of ethoxy groups to ethanol and Cu–O bridge.[77]

Step-4 – At some critical point, the super saturated clusters of these Cu complexes form a gel (step 4 in Fig. 8) which further undergoes elimination reactions to form by-products such as water and ethanol molecules, as shown in eqn (6) and (7) respectively. This results in basic units of Cu–O–Cu bridges that form the square planar CuO_4 units (square planar structure in which divalent copper is in the centre between four oxygen corners), the fundamental unit of the monoclinic CuO crystal lattice. CuO QDs growth takes place *via* the progression of CuO_4 units in all six different directions and depends on the availability of monomeric precursors.[75] The 3-dimensional branching required to sustain the growth process is possible also in the presence of H_2O_2. Thus, the process of polycondensation occurs locally by the gel and ends up as nucleates. We should note that in these reaction schemes, ethanol is not consumed and merely acts as an intermediate reactant which is re-formed at the end of the reaction chain. We also know that water (hydrogen peroxide) concentrations are in general lower (not increasing) when CuO QDs are synthesized (*i.e.* with Cu foil anode *vs.* graphite anode), suggesting that H_2O (H_2O_2) participate in the reactions leading to the QDs synthesis as per our analysis.

The synthesis rate and size control of CuO QDs during PiNE is determined by the spatial distribution of species due to the microplasma interacting with the liquid. The reaction volume inside the liquid phase underneath the plasma appears to possess suitable conditions such as monomer concentration for spontaneous nucleation and growth of QDs. Therefore, the formation of QDs occurs within a very localized region near the plasma, in comparison to other synthesis techniques where growth occur across the entire solution.[78] The diffusion of QDs away from this region (possibly facilitated by temperature gradients and gas flow induced convection/advection) terminates the growth of the QDs. The growth process is therefore restricted near the plasma interface where there is rich availability of all precursor and reactant for rapid formation of QDs (step 4 in Fig. 8).

This analysis implies that QD size is determined by the reaction volume under the plasma and diffusion time of the QDs out of this region. This is confirmed by the increase in number density of the QDs over time (Fig. 6c), which does not alter the QDs diameter (same bandgap as per results above). The non-Gaussian and skewed size distribution (Fig. 2a) provide strong evidence that growth and size are determined by the residence time rather than from monomer concentration typical of batch processes. Finally, the absence of copper ethoxide but increasing concentrations of Cu ions, water and hydrogen peroxide suggest that the QDs formation rate is limited by the supply of ethoxy ions produced by electron-induced dissociative attachment (reaction (22) in Table S4 in section 12 of ESI†), which in turn depend on the electron flux and therefore the electrical current at the plasma–ethanol interface. At first this would mean that increasing the electron flux, *i.e.* current (ESI, Fig. S2†), we should be able to increase the growth rate and produce larger particles. However, this is not the case as the increased interface electron current also

promotes competitor reactions whereby enhanced levels of hydrogen peroxide and water capture Cu ethoxy to form amorphous gelatine compounds as observed by TEM (Fig. S7a, section 2†). At 3 mA, a higher production of Cu ions from anodization and hydrogen peroxide can lead to a bottleneck in step-4 therefore extending the gelation network and affecting growth of nucleates. However, at the same time, the presence of protonic species as evident from the increase in acidity of the solution could also prevent the hydrolysis of the cluster gel to form nucleates.[79] Overall, it can be concluded that the process of formation of CuO QDs is very localised near the plasma interface with the liquid, where the formation of QDs is aided mainly by the presence of water molecules, organo-metallic compounds, chiefly copper ethoxide, and moderately by the presence of hydrogen peroxide, supporting the idea of green cycle mechanism.

Conclusion

The formation mechanisms of metal oxide QDs in a PINE process were studied in detail providing a clearer understanding of the reaction paths. Various primary analytical techniques including FTIR and NMR spectroscopies, as well as GC-MS, confirmed the presence of solvent as the major component after plasma process except some by-products such as water, hydrogen peroxide and IPA, which were found to exist along with the Cu-oxide QDs. These chemical species were also quantified. Further, a detailed CuO QD synthesis cycle was drawn based on observed products and assuming the key copper based organo-metallic complexes. A full understanding of the green cyclic reaction paths was therefore achieved and will help in devising optimization steps. For instance, tuning the process parameters can lead to a more accurate supply of copper ions, water molecules and controlled production of hydrogen peroxide. This all-together can improve yields and therefore minimize energy consumption. We foresee energy consumption as one of the key aspects that will require investigation and optimization before this process can become an attractive industrial opportunity. The process may be similar for the generalized synthesis of a wider range of metal oxide nanoparticles and QDs. Indeed, this work contributes to the understanding of plasma–liquid interaction, specifically with ethanol, which could be highly relevant to build a more complete theoretical framework for PINE.

Conflicts of interest

The authors declare no conflict of interests.

Acknowledgements

This work was supported by EPSRC (EP/M024938/1). We would like to thank Dr Darragh Carolan for carrying out TEM and XPS measurements.

References

1 K. Harada and S. Suzuki, *Nature*, 1977, **266**, 275–276.
2 J. Gubkin, *Ann. Phys. Chem.*, 1887, **268**, 114–115.
3 P. Rumbach, D. M. Bartels, R. M. Sankaran and D. B. Go, *Nat. Commun.*, 2015, **6**, 7248.
4 R. Hawtof, S. Ghosh, E. Guarr, C. Xu, R. Mohan Sankaran and J. N. Renner, *Sci. Adv.*, 2019, **5**, eaat5778.
5 C. Richmonds, M. Witzke, B. Bartling, S. W. Lee, J. Wainright, C.-C. Liu and R. M. Sankaran, *J. Am. Chem. Soc.*, 2011, **133**, 17582–17585.
6 P. Rumbach, M. Witzke, R. M. Sankaran and D. B. Go, *J. Am. Chem. Soc.*, 2013, **135**, 16264–16267.
7 A. Mota-Lima, J. F. do Nascimento, O. Chiavone-Filho and C. A. O. Nascimento, *J. Phys. Chem. C*, 2019, **123**, 21896–21912.
8 H. Jablonowski and T. von Woedtke, *Clin. Plasma Med.*, 2015, **3**, 42–52.
9 K. Oehmigen, M. Hähnel, R. Brandenburg, C. Wilke, K.-D. Weltmann and T. von Woedtke, *Plasma Processes Polym.*, 2010, **7**, 250–257.
10 P. Shaw, N. Kumar, H. S. Kwak, J. H. Park, H. S. Uhm, A. Bogaerts, E. H. Choi and P. Attri, *Sci. Rep.*, 2018, **8**, 11268.
11 W. Chiang, D. Mariotti, R. M. Sankaran, J. G. Eden and K. Ostrikov, *Adv. Mater.*, 2020, **32**, 1905508.
12 D. Mariotti, J. Patel, V. Švrček and P. Maguire, *Plasma Processes Polym.*, 2012, **9**, 1074–1085.
13 M. R. Webb and G. M. Hieftje, *Anal. Chem.*, 2009, **81**, 862–867.
14 S. Mitra, V. Švrček, D. Mariotti, T. Velusamy, K. Matsubara and M. Kondo, *Plasma Processes Polym.*, 2014, **11**, 158–163.
15 A. R. Denaro and A. Hickling, *J. Electrochem. Soc.*, 1958, **105**, 265.
16 Q. Chen, J. Li and Y. Li, *J. Phys. D: Appl. Phys.*, 2015, **48**, 424005.
17 P. Maguire, D. Rutherford, M. Macias-Montero, C. Mahony, C. Kelsey, M. Tweedie, F. Pérez-Martin, H. McQuaid, D. Diver and D. Mariotti, *Nano Lett.*, 2017, **17**, 1336–1343.
18 G. Saito, S. Hosokai, M. Tsubota and T. Akiyama, *Cryst. Growth Des.*, 2012, **12**, 2455–2459.
19 D. Mariotti and R. M. Sankaran, *J. Phys. D: Appl. Phys.*, 2010, **43**, 323001.
20 D. Sun, J. Turner, N. Jiang, S. Zhu, L. Zhang, B. G. Falzon, C. P. McCoy, P. Maguire, D. Mariotti and D. Sun, *Compos. Sci. Technol.*, 2020, **186**, 107911.
21 D. Sun, M. Tang, L. Zhang, B. G. Falzon, D. B. Padmanaban, D. Mariotti, P. Maguire, H. Xu, M. Chen and D. Sun, *Nanotechnology*, 2019, **30**, 455603.
22 T. Velusamy, A. Liguori, M. Macias-Montero, D. B. Padmanaban, D. Carolan, M. Gherardi, V. Colombo, P. Maguire, V. Svrcek and D. Mariotti, *Plasma Processes Polym.*, 2017, **14**, 1600224.
23 C. Ni, D. Carolan, C. Rocks, J. Hui, Z. Fang, D. B. Padmanaban, J. Ni, D. Xie, P. Maguire, J. T. S. Irvine and D. Mariotti, *Green Chem.*, 2018, **20**, 2101–2109.
24 S. Chakrabarti, D. Carolan, B. Alessi, P. Maguire, V. Svrcek and D. Mariotti, *Nanoscale Adv.*, 2019, **1**, 4915–4925.

25 C. Ni, D. Carolan, J. Hui, C. Rocks, D. Padmanaban, J. Ni, D. Xie, Z. Fang, J. Irvine, P. Maguire and D. Mariotti, *Cryst. Growth Des.*, 2019, **19**, 5249–5257.
26 K. Zhou, R. Wang, B. Xu and Y. Li, *Nanotechnology*, 2006, **17**, 3939–3943.
27 Y.-F. Lim, J. J. Choi and T. Hanrath, *J. Nanomater.*, 2011, **2012**, 1–6.
28 L. B. Kong, Y. Z. Huang, W. X. Que, T. S. Zhang, S. Li, J. Zhang, Z. L. Dong and D. Y. Tang, *Transparent Ceramics*, Springer International Publishing, Cham, 2015, pp. 29–91.
29 D. P. Dubal, D. S. Dhawale, R. R. Salunkhe, V. S. Jamdade and C. D. Lokhande, *J. Alloys Compd.*, 2010, **492**, 26–30.
30 Y. Ge, Z. H. Shah, C. Wang, J. Wang, W. Mao, S. Zhang and R. Lu, *ACS Appl. Mater. Interfaces*, 2015, **7**, 26437–26444.
31 H. T. Zhu, C. Y. Zhang, Y. M. Tang and J. X. Wang, *J. Phys. Chem. C*, 2007, **111**, 1646–1650.
32 X. Zhang, G. Wang, X. Liu, J. Wu, M. Li, J. Gu, H. Liu and B. Fang, *J. Phys. Chem. C*, 2008, **112**, 16845–16849.
33 D. Su, X. Xie, S. Dou and G. Wang, *Sci. Rep.*, 2014, **4**, 5753.
34 L. Mandal, K. R. Yang, M. R. Motapothula, D. Ren, P. Lobaccaro, A. Patra, M. Sherburne, V. S. Batista, B. S. Yeo, J. W. Ager, J. Martin and T. Venkatesan, *ACS Appl. Mater. Interfaces*, 2018, **10**, 8574–8584.
35 B. Fang, Y. Xing, A. Bonakdarpour, S. Zhang and D. P. Wilkinson, *ACS Sustainable Chem. Eng.*, 2015, **3**, 2381–2388.
36 B. Talluri, E. Prasad and T. Thomas, *Superlattices Microstruct.*, 2018, **113**, 600–607.
37 R. Vijaya Kumar, Y. Diamant and A. Gedanken, *Chem. Mater.*, 2000, **12**, 2301–2305.
38 M. Vaseem, A. Umar, S. H. Kim and Y. B. Hahn, *J. Phys. Chem. C*, 2008, **112**, 5729–5735.
39 G. Qiu, S. Dharmarathna, Y. Zhang, N. Opembe, H. Huang and S. L. Suib, *J. Phys. Chem. C*, 2012, **116**, 468–477.
40 M. Outokesh, M. Hosseinpour, S. J. Ahmadi, T. Mousavand, S. Sadjadi and W. Soltanian, *Ind. Eng. Chem. Res.*, 2011, **50**, 3540–3554.
41 J. D. Aiken and R. G. Finke, *J. Mol. Catal. A: Chem.*, 1999, **145**, 1–44.
42 C. E. Carraher, *Introduction to Polymer Chemistry*, CRC Press, 4th edn, 2017.
43 Z. Singh and I. Singh, *Sci. Rep.*, 2019, **9**, 5880.
44 I. Singh and R. K. Bedi, *Solid State Sci.*, 2011, **13**, 2011–2018.
45 G. Bozkurt, A. Bayrakçeken and A. K. Özer, *Appl. Surf. Sci.*, 2014, **318**, 244–250.
46 NIST XPS Database, Selected Element Search Result, https://srdata.nist.gov/xps/EngElmSrchQuery.aspx?EType=PE&CSOpt=Retri_ex_dat&Elm=Mn, (accessed 4 March 2019).
47 E. Andreoli, D. A. Rooney, W. Redington, R. Gunning and C. B. Breslin, *J. Phys. Chem. C*, 2011, **115**, 8725–8734.
48 I. C. Hwang and S. I. Woo, *J. Phys. Chem. B*, 1997, **101**, 4055–4059.
49 R. P. Vasquez, *Surf. Sci. Spectra*, 1998, **5**, 257–261.
50 R. M. Silverstein and F. X. Webster, *Spectrometric identification of organic compounds*, Wiley, 1998.
51 P. Zarzycki and J. R. Rustad, *J. Phys. Chem. A*, 2009, **113**, 291–297.
52 N. R. Babij, E. O. McCusker, G. T. Whiteker, B. Canturk, N. Choy, L. C. Creemer, C. V. De Amicis, N. M. Hewlett, P. L. Johnson, J. A. Knobelsdorf, F. Li, B. A. Lorsbach, B. M. Nugent, S. J. Ryan, M. R. Smith and Q. Yang, *Org. Process Res. Dev.*, 2016, **20**, 661–667.
53 H. E. Gottlieb, V. Kotlyar and A. Nudelman, *J. Org. Chem.*, 1997, **62**, 7512–7515.
54 L. N. Kashapov, N. F. Kashapov and R. N. Kashapov, *J. Phys.: Conf. Ser.*, 2013, **479**, 012011.
55 A. P. Abbott, G. Frisch, J. Hartley, W. O. Karim and K. S. Ryder, *Prog. Nat. Sci.: Mater. Int.*, 2015, **25**, 595–602.
56 P. Bruggeman, E. Ribežl, A. Maslani, J. Degroote, A. Malesevic, R. Rego, J. Vierendeels and C. Leys, *Plasma Sources Sci. Technol.*, 2008, **17**, 025012.
57 C.-W. Chen, H.-M. Lee and M.-B. Chang, *J. Electrostat.*, 2009, **67**, 703–708.
58 F. Liu, P. Sun, N. Bai, Y. Tian, H. Zhou, S. Wei, Y. Zhou, J. Zhang, W. Zhu, K. Becker and J. Fang, *Plasma Processes Polym.*, 2010, **7**, 231–236.
59 S. Ikawa, K. Kitano and S. Hamaguchi, *Plasma Processes Polym.*, 2010, **7**, 33–42.
60 C W Chen, H-M Lee and M B Chang, *IEEE Trans. Plasma Sci.*, 2008, **36**, 215–219.
61 R. Burlica, M. J. Kirkpatrick and B. R. Locke, *J. Electrostat.*, 2006, **64**, 35–43.
62 M. Falk, *J. Raman Spectrosc.*, 1990, **21**, 563–567.
63 D. Mariotti, V. Švrček, J. W. J. Hamilton, M. Schmidt and M. Kondo, *Adv. Funct. Mater.*, 2012, **22**, 954–964.
64 Z. C. Liu, D. X. Liu, C. Chen, D. Li, A. J. Yang, M. Z. Rong, H. L. Chen and M. G. Kong, *J. Phys. D: Appl. Phys.*, 2015, **48**, 495201.
65 M. A. Almubarak, *J. Electrochem. Soc.*, 1977, **124**, 1356.
66 C. Du, J. Mo and H. Li, *Chem. Rev.*, 2015, **115**, 1503–1542.
67 C. Du, J. Mo, J. Tang, D. Huang, Z. Mo, Q. Wang, S. Ma and Z. Chen, *Appl. Energy*, 2014, **133**, 70–79.
68 C. Du, D. Ma, J. Wu, Y. Lin, W. Xiao, J. Ruan and D. Huang, *Int. J. Hydrogen Energy*, 2015, **40**, 15398–15410.
69 M. Witzke, P. Rumbach, D. B. Go and R. M. Sankaran, *J. Phys. D: Appl. Phys.*, 2012, **45**, 442001.
70 R. Burlica, K.-Y. Shih and B. R. Locke, *Ind. Eng. Chem. Res.*, 2010, **49**, 6342–6349.
71 J. W. Larson, P. Cerutti, H. K. Garber and L. G. Hepler, *J. Phys. Chem.*, 1968, **72**, 2902–2907.
72 G. R. Lee and J. A. Crayston, *Adv. Mater.*, 1993, **5**, 434–442.
73 L. L. Hench and J. K. West, *Chem. Rev.*, 1990, **90**, 33–72.
74 B. E. Yoldas, *J. Mater. Sci.*, 1986, **21**, 1087–1092.
75 Y. Cudennec and A. Lecerf, *Solid State Sci.*, 2003, **5**, 1471–1474.
76 C. H. Brubaker and M. Wicholas, *J. Inorg. Nucl. Chem.*, 1965, **27**, 59–62.
77 C. Sanchez, J. Livage, M. Henry and F. Babonneau, *J. Non-Cryst. Solids*, 1988, **100**, 65–76.
78 N. T. K. Thanh, N. Maclean and S. Mahiddine, *Chem. Rev.*, 2014, **114**, 7610–7630.
79 M. L. Tobe, *Acc. Chem. Res.*, 1970, **3**, 377–385.